ELSEVIER

NeuroImage

www.elsevier.com/locate/ynimg
NeuroImage 42 (2008) 122–134

Towards better MR characterization of neural tissues using directional diffusion kurtosis analysis

Edward S. Hui,[a,b] Matthew M. Cheung,[a,b] Liqun Qi,[c] and Ed X. Wu[a,b,*]

[a]*Laboratory of Biomedical Imaging and Signal Processing, The University of Hong Kong, Pokfulam, Hong Kong*
[b]*Department of Electrical and Electronic Engineering, The University of Hong Kong, Pokfulam, Hong Kong*
[c]*Department of Applied Mathematics, The Hong Kong Polytechnic University, Hung Hom, Kowloon, Hong Kong*

Received 20 December 2007; revised 14 April 2008; accepted 17 April 2008
Available online 30 April 2008

MR diffusion kurtosis imaging (DKI) was proposed recently to study the deviation of water diffusion from Gaussian distribution. Mean kurtosis, the directionally averaged kurtosis, has been shown to be useful in assessing pathophysiological changes, thus yielding another dimension of information to characterize water diffusion in biological tissues. In this study, orthogonal transformation of the 4th order diffusion kurtosis tensor was introduced to compute the diffusion kurtoses along the three eigenvector directions of the 2nd order diffusion tensor. Such axial ($K_{//}$) and radial ($K_{\perp}$) kurtoses measured the kurtoses along the directions parallel and perpendicular, respectively, to the principal diffusion direction. DKI experiments were performed in normal adult ($N=7$) and formalin-fixed rat brains ($N=5$). DKI estimates were documented for various white matter (WM) and gray matter (GM) tissues, and compared with the conventional diffusion tensor estimates. The results showed that kurtosis estimates revealed different information for tissue characterization. For example, $K_{//}$ and $K_{\perp}$ under formalin fixation condition exhibited large and moderate increases in WM while they showed little change in GM despite the overall dramatic decrease of axial and radial diffusivities in both WM and GM. These findings indicate that directional kurtosis analysis can provide additional microstructural information in characterizing neural tissues.

Keywords: Water diffusion; Diffusion kurtosis; Directional kurtosis; Diffusion kurtosis tensor; DKI; Non-Gaussian diffusion; Restricted diffusion; Orthogonal transformation

Introduction

Diffusion kurtosis imaging (DKI) was recently proposed to characterize the non-Gaussian water diffusion behavior in neural tissues (Fieremans et al., 2008; Jensen et al., 2005; Lu et al., 2006). Biological tissues are heterogeneous in nature comprising multiple compartments (Le Bihan, 1991). Thus the Gaussian distribution generally assumed for free or unrestricted water diffusion is insufficient to describe the diffusion process in biological environment (Karger, 1985). In addition, the dependency of diffusion-weighted (DW) signal on *b*-value has been observed to be non-monoexponential in neural tissues (Basser and Jones, 2002; Mulkern et al., 1999; Niendorf et al., 1996). To characterize such non-Gaussian diffusion behavior, kurtosis, the 4th central moment of the diffusion distribution (Balanda and Macgillivray, 1988), was introduced (Jensen et al., 2005). It is a dimensionless measure that can be either positive or negative. Positive kurtosis means that distribution is more sharply peaked than Gaussian. The higher the diffusion kurtosis, the more the water molecule diffusion deviates from Gaussian distribution, indicative of a more restricted diffusion environment. Apparent diffusion kurtosis has been estimated by acquiring DW signals at multiple *b*-values up to a maximum of 2500 s/mm^2 in humans (Jensen et al., 2005; Lu et al., 2006). Because the 4th order diffusion kurtosis tensor (KT) is fully symmetric and has 15 independent components, DKI experiments are typically performed in more than 15 directions to obtain the full KT.

Several approaches have been proposed to study the non-monoexponential diffusion behavior. They include the multi-compartment model (Clark et al., 2002), statistical diffusion model (Yablonskiy et al., 2003), generalized diffusion tensors (Liu et al., 2004; Ozarslan and Mareci, 2003) and q-space imaging (Callaghan, 1991). Among them, q-space imaging, in which water diffusion displacement probability profile is estimated, is deemed to provide a robust characterization of the diffusion related structural changes in diseased neural tissues (Assaf et al., 2005, 2003; Biton et al., 2006; Nossin-Manor et al., 2007). Despite of the advantage of quantitatively measuring the water displacement, q-space imaging often requires a long scan time, large *b*-values and a strong gradient. The DKI approach largely circumvents these limitations, offering a more practical means to investigate the non-Gaussian diffusion behavior with relative ease and reasonable speed. It utilizes the non-monoexponential dependence of DW signals on *b*-values to map the diffusion kurtosis as a biomarker for microstructural changes in various neural tissues, including both white and gray matters.

* Corresponding author. Laboratory of Biomedical Imaging and Signal Processing, Department of Electrical and Electronic Engineering, The University of Hong Kong, Pokfulam, Hong Kong. Fax: +852 2559 8738.
E-mail address: ewu@eee.hku.hk (E.X. Wu).
Available online on ScienceDirect (www.sciencedirect.com).

1053-8119/$ - see front matter © 2008 Elsevier Inc. All rights reserved.
doi:10.1016/j.neuroimage.2008.04.237

Recent experimental findings in human DKI studies were promising (Falangola et al., 2007a,b; Helpern et al., 2007; Jensen et al., 2005; Lu et al., 2006; Ramani et al., 2007). Mean kurtosis (*MK*), the average apparent kurtosis along all diffusion gradient encoding directions, was measured and demonstrated to offer an improved sensitivity in detecting developmental and pathological changes in neural tissues as compared to the conventional diffusion tensor imaging (DTI). One might argue that by simply taking the mean of the apparent kurtoses measured along all diffusion directions it would reduce the sensitivity and specificity in probing diffusion kurtosis change occurring along a specific direction, for instance, parallel or perpendicular to the principal diffusion eigenvector as denoted as axial or radial direction, respectively. Given that axial and radial diffusivity analyses have been successfully employed in numerous studies to elucidate the specific neural tissue pathologies in animal models (Song et al., 2003, 2002; Sun et al., 2006) and humans (Trip et al., 2006), it is valuable to analyze the directional kurtoses by obtaining the water diffusion kurtoses along these two directions. Such directional diffusion kurtosis analysis may provide unique and complementary information regarding the biological systems, thus improving the MR diffusion characterization of neural tissues in normal, developmental or pathological states.

In this study, an orthogonal transformation of the 4th order KT was proposed to compute the diffusion kurtoses along the directions of the three diffusion eigenvectors. Histological fixation is known to alter the cellular structure and hence the restriction to water diffusion (Does et al., 2003; Schwartz et al., 2005; Takahashi et al., 2002; Thelwall et al., 2006; Yong-Hing et al., 2005), likely leading to varying extents of water diffusion restriction along the axial and radial directions. Therefore, DKI experiments were performed in both normal and formalin-fixed adult rat brains to document both DKI and DTI estimates in various brain tissues, and to evaluate whether directional kurtosis analysis improves tissue characterization.

Materials and methods

Theory

In conventional DTI, the 2nd order diffusion tensor (DT) is fully characterized by its eigenvalues (λ_i with i=1, 2 3 and $\lambda_1>\lambda_2>\lambda_3$) and the corresponding orthonormal eigenvectors that can be obtained by matrix diagonalization (Basser et al., 1994). In DKI (Jensen et al., 2005; Lu et al., 2006), both apparent diffusion coefficient (D_{app}) and apparent diffusion kurtosis (K_{app}) along each applied diffusion gradient direction are estimated together by fitting the following equation with the multiple DW signals acquired using a range of b-values:

$$\ln[S(b)/S(0)] \approx -bD_{\text{app}} + \frac{1}{6}b^2 D_{\text{app}}^2 K_{\text{app}}, \tag{1}$$

where $S(b)$ is the DW signal intensity at a particular b-value, and $S(0)$ the signal without applying any diffusion gradient. To obtain reliable curve fitting, a sufficient b-value range must be chosen to permit as much non-monoexponential decay as possible. It is noteworthy that the kurtosis formulation above is valid only for a limited b-value range because the quadratic term $-bD_{\text{app}} + \frac{1}{6}b^2 D_{\text{app}}^2 K_{\text{app}}$ will increase with b-value after the minima. Therefore, b-values chosen to fit Eq. (1) should be smaller than $b_{\text{minima}} = 3/(D_{\text{app}} K_{\text{app}})$.

The mean kurtosis (*MK*) is measured as:

$$MK = \frac{1}{n}\sum_{i=1}^{n} (K_{\text{app}})_i, \tag{2}$$

where $(K_{\text{app}})_i$ is the K_{app} along i^{th} direction and n is the total number of directions in which diffusion measurements are carried out. K_{app} at a particular direction is related to a 4th order kurtosis tensor (*KT*) by:

$$K_{\text{app}} = \frac{MD^2}{D_{\text{app}}^2} \cdot \sum_{i=1}^{3}\sum_{j=1}^{3}\sum_{k=1}^{3}\sum_{l=1}^{3} n_i n_j n_k n_l W_{ijkl}, \tag{3}$$

where mean diffusivity is $MD = \frac{1}{3}\sum_{i=1}^{3}\lambda_i$, n_i the component of the diffusion encoding gradient unit vector and W_{ijkl} the individual element of *KT*. Note that *KT* has 15 independent elements only due to the symmetry of different diffusion processes probed by MR. Because of the mathematical complexity of the 4th order tensor (Qi, 2005), individual *KT* elements, eigenvalues and eigenvectors are yet to be explored in terms of their direct physical relevance to the diffusion processes. Nevertheless, KT can be transformed from the standard Cartesian coordinate system to another coordinate system in which the 3 orthonormal eigenvectors of DT are the base coordinate vectors by (Qi et al., in press):

$$\hat{W}_{ijkl} = \sum_{i'=1}^{3}\sum_{j'=1}^{3}\sum_{k'=1}^{3}\sum_{l'=1}^{3} e_{ii'} e_{jj'} e_{kk'} e_{ll'} W_{i'j'k'l'}. \tag{4}$$

From Eqs. (3) and (4), the kurtosis along the individual DT eigenvector is:

$$K_i = \frac{MD^2}{\lambda_i^2} \cdot \hat{W}_{iiii}. \tag{5}$$

Thus the axial ($K_{//}$) and radial kurtosis ($K\perp$) can be obtained from the three newly derived kurtoses:

$$K_{//} = K_1 \tag{6}$$

$$K_{\perp} = \frac{K_2 + K_3}{2}. \tag{7}$$

Note that these two directional kurtoses are not related to *MK* by simple linear combination, i.e., $MK \neq (K_{//} + 2K\perp)/3$, because the 3D distribution of the 4th order kurtosis tensor cannot be simply represented as an ellipsoid. In conventional DTI, however, *MD* is related directly to the axial diffusivity ($\lambda_{//}$) and radial diffusivity ($\lambda\perp$) by $MD = (\lambda_{//} + 2\lambda\perp)/3$ owing to the nature of 2nd order diffusion tensor where three eigenvalues represent the diffusion coefficients along three orthogonal eigenvectors. To examine the anisotropy of these directional kurtoses, the fractional anisotropy of kurtosis (FA_K) can also be conveniently defined in a way similar to that in DTI (Basser and Pierpaoli, 1996) as:

$$FA_K = \sqrt{\frac{3}{2} \cdot \frac{(K_1 - \overline{K})^2 + (K_2 - \overline{K})^2 + (K_3 - \overline{K})^2}{K_1^2 + K_2^2 + K_3^2}}, \tag{8}$$

where $\overline{K} = \frac{1}{3}\sum_{i=1}^{3} K_i$.

In vivo and ex vivo rat brain DKI

All MRI experiments were performed on a 7 T scanner with a maximum gradient of 360 mT/m (70/16 PharmaScan, Bruker Biospoin GmbH, Germany). In vivo DKI was carried out on normal 10-month-old Sprague–Dawley rats (N=7, 250–350 g). During imaging, animals were anesthetized with isoflurane/air at 3% for induction and 1.5% for maintenance via a nose cone. A birdcage transmit-only RF coil with 72 mm inner diameter was used in combination with an actively decoupled receive-only quadrature surface coil. DW images were acquired with a respiration-gated spin echo 4-shot EPI sequence with the implementation of navigator echo for correcting $N/2$ ghost, frequency and phase shifts between shots. An encoding scheme of 30 gradient directions (Jones et al., 1999) was

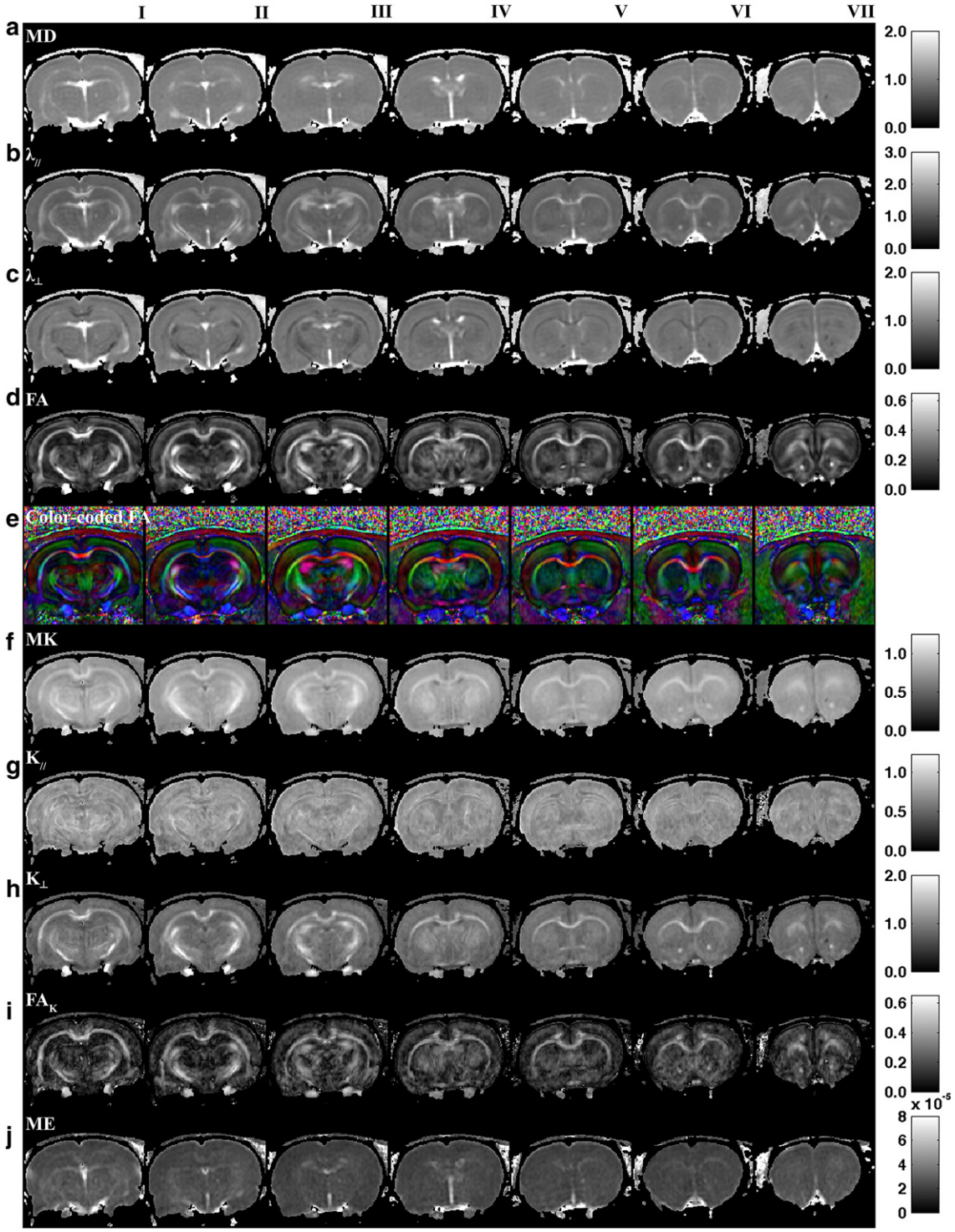

Fig. 1. Slice I to VII of the typical (a) *MD*, (b) $\lambda_{//}$, (c) $\lambda_{\perp}$, (d) *FA*, (e) *FA* direction, (f) *MK*, (g) $K_{//}$, (h) $K_{\perp}$, (i) FA_K and (j) normalized curve-fitting mean error (ME) maps from an in vivo adult rat brain. *FA* direction has the color coding of red for left–right, green for top–bottom and blue for in–out direction.

implemented to acquire DW images. Five additional images with $b=0$ (B_0 images) were also acquired. The sequence parameters were: TR/TE=3000/30.3 ms, $\delta/\Delta=5/17$ ms, slice thickness=1 mm (0.1 mm slice gap), FOV=30 mm, data matrix=128×128 (zero filled to 256×256) and image resolution 234×234 μm^2. Five b-values were used for each gradient direction (0.5, 1.0, 1.5, 2.0 and 2.5 ms/μm^2). Such b-values were chosen to allow sufficient non-monoexponential decay of DW signals, but they were smaller than b_{minima} estimated from the mean kurtosis values reported in the previous human study (Lu et al., 2006). The sequence was repeated 4 times for signal averaging, resulting in a total acquisition time of approximately 120 min depending on the respiratory rate. Seven coronal slices covering from 2.6 to −5.1 mm of bregma were acquired. To ensure reproducible slice location, coronal slices were planned with reference

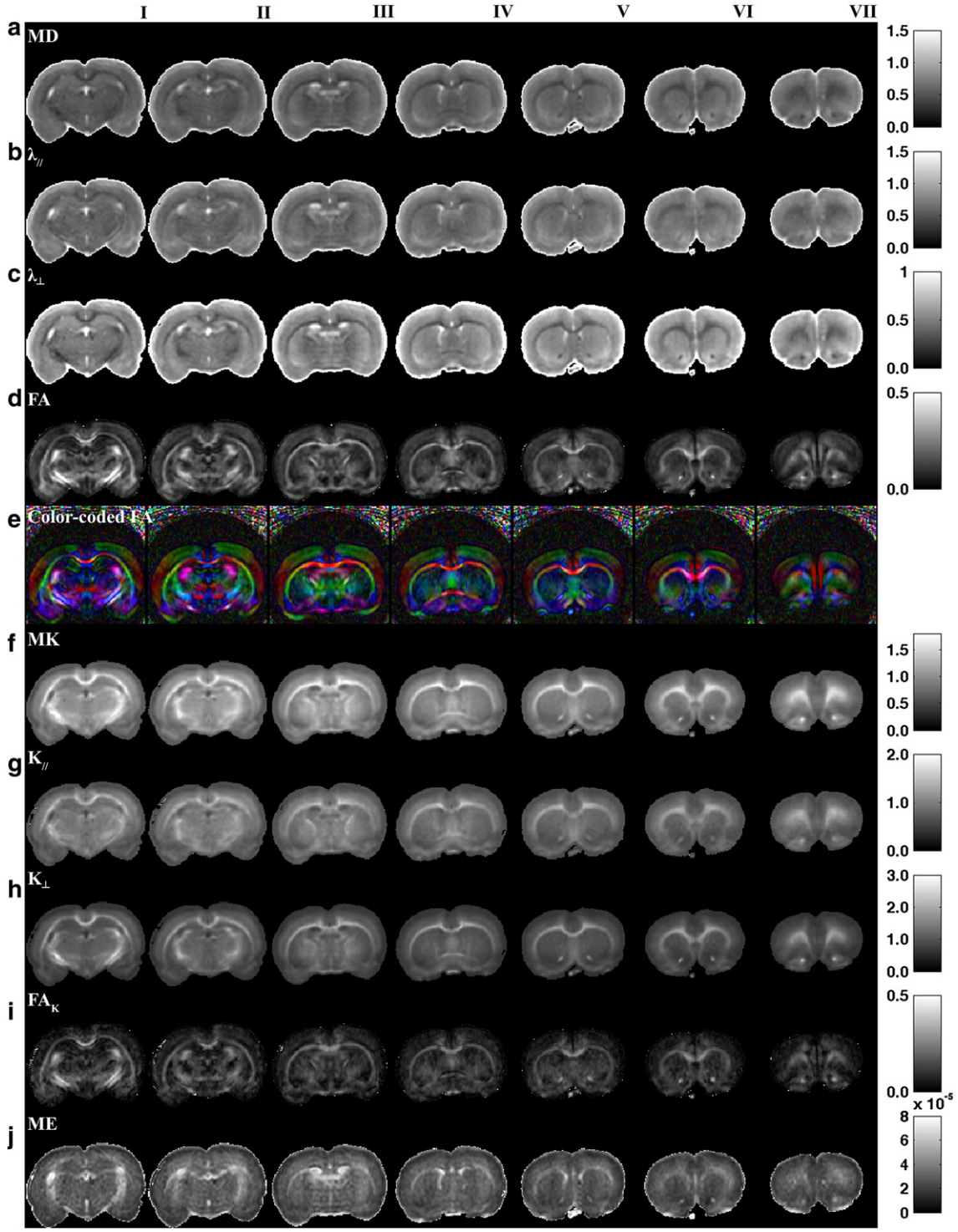

Fig. 2. Slice I to VII of the typical (a) *MD*, (b) $\lambda_{//}$, (c) $\lambda_{\perp}$, (d) *FA*, (e) *FA* direction, (f) *MK*, (g) $K_{//}$, (h) $K_{\perp}$, (i) FA_K and (j) ME maps from an formalin-fixed ex vivo adult rat brain sample.

to the corpus callosum (CC) on the central T2-weighted sagittal image (Paxinos and Watson, 2005). The slice stack direction was first made parallel to the CC, and then rotated clockwise by 18°.

For ex vivo DKI experiments, normal 10-month-old Sprague–Dawley rats (N=5, 200–320 g) were anesthetized with intraperitoneal injection of ketamine (64 mg/kg) and xylazine (7 mg/kg), and then perfused transcardially with 10% formaldehyde. Brains were excised and fixed first in 10% formaldehyde for 24 h and then in 70% ethanol. Afterwards, they were suspended by 1% agarose gel in plastic tubes (20 mm outer diameter) for MRI at ~20 °C. DKI was performed using a 23-mm birdcage quadrature RF coil for both transmitting and receiving. All acquisition parameters were the same as those for in vivo experiments except for the followings: TE=34.3 ms, δ=9 ms, and b-values of 1.0, 2.0, 3.0, 4.0 and 5.0 ms/μm^2. Note that a larger b-value range was employed here for ex vivo experiments because the mean and directional diffusivities in rodent brains decrease substantially under formalin fixation (Sun et al., 2005; Sun et al., 2003).

Data analysis

DW images were first co-registered using AIR5.2.5 (Woods et al., 1998). DW signals acquired with different b-values were fitted to Eq. (1) for D_{app} and K_{app} along each diffusion direction. Both DT and KT were computed following the procedures described earlier (Lu et al., 2006). *MK*, $K_{//}$, $K\perp$ and FA_K maps were calculated. *MD*, *FA*, $\lambda_{//}$ (=λ_1) and $\lambda\perp$ (=[λ_2+λ_3]/2) maps (Basser and Pierpaoli, 1996; Song et al., 2003) were also obtained for comparison. In addition, the overall normalized mean error (ME) map of the curve fitting to 6 b-values among 30 directions was computed, i.e. $ME = \left(\sum_{j=1}^{30}\sqrt{\sum_{i=1}^{6} r_{ij}^2}\right) / \left(\sum_{j=1}^{30}\sqrt{\sum_{i=1}^{6} y_{ij}^2}\right)$ where $r_{ij}=y_{ij}'-y_{ij}$, y_{ij} the element i of raw data in j^{th} direction and y_{ij}' the fitted data.

Multi-slice regions of interest (ROIs) were manually drawn by referencing to the standard rat brain atlas (Paxinos and Watson, 2005). Anatomical landmarks were found from the *FA* and *MK* maps in each animal. Four white matter (WM) tissues, namely CC, external capsule (EC), cerebral peduncle (CP) and anterior commissure (AC), and 3 gray matter (GM) tissues, namely cerebral cortex (CT), hippocampus (HP) and cauduate putamen (CPu) were defined. *MD*, $\lambda_{//}$, $\lambda\perp$, *FA*, *MK*, $K_{//}$, $K\perp$ and FA_K, were then measured by volume-averaging the multi-slice ROIs for each tissue. The percentage changes of these estimates from in vivo to ex vivo were also calculated. To reveal the potential relationship between the DKI estimates and the conventional DTI estimates, scatter plots of *MK* vs. *MD*, $K_{//}$ vs. $\lambda_{//}$, $K\perp$ vs. $\lambda\perp$, and FA_K vs. *FA* were made for both in vivo and ex vivo data. Correlation testing was performed using Spearman-rho analysis to determine whether DKI estimates led to independent measurements.

Results

DTI- and DKI-derived parametric maps

Figs. 1 and 2 illustrate the typical *MD*, $\lambda_{//}$, $\lambda\perp$, *FA*, color-coded *FA* direction, *MK*, $K_{//}$, $K\perp$, FA_K and ME maps from an intact in vivo rat brain and a formalin-fixed ex vivo rat brain, respectively, with Fig. 3 showing the maps from the first slice only. Different contrasts were generally observed between various DTI and DKI maps, particularly between the directional diffusivity and kurtosis maps. The image contrasts of both DTI- and DKI-derived parametric maps were found to alter under formalin fixation. In general, *MK* and $K\perp$ maps exhibited strong contrasts between WM and GM tissues under both in vivo and ex vivo conditions. As for $K_{//}$, relatively less contrast was seen between WM and GM in vivo (Fig. 1f) while a strong contrast was observed under ex vivo

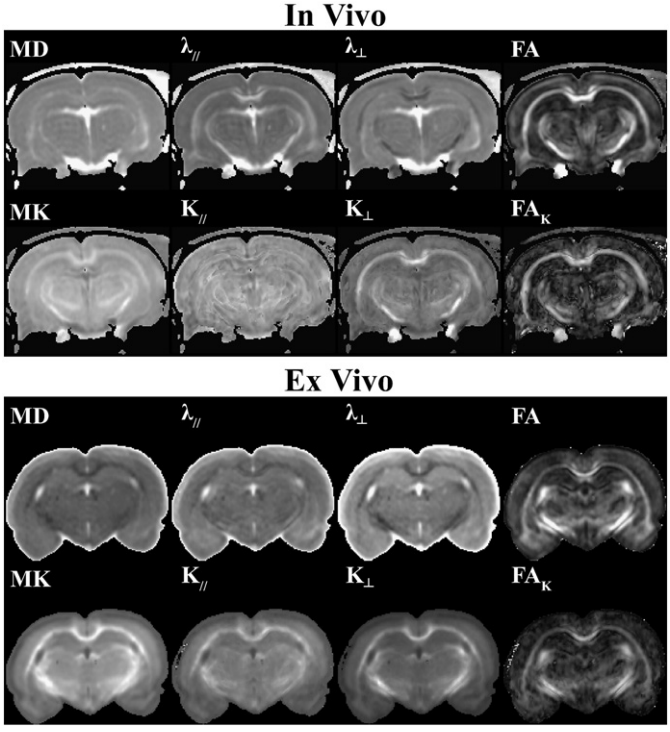

Fig. 3. *MD*, $\lambda_{//}$, $\lambda\perp$, *FA*, *MK*, $K_{//}$, $K\perp$ and FA_K maps of the slice I of the in vivo and ex vivo brains shown in Figs. 1 and 2.

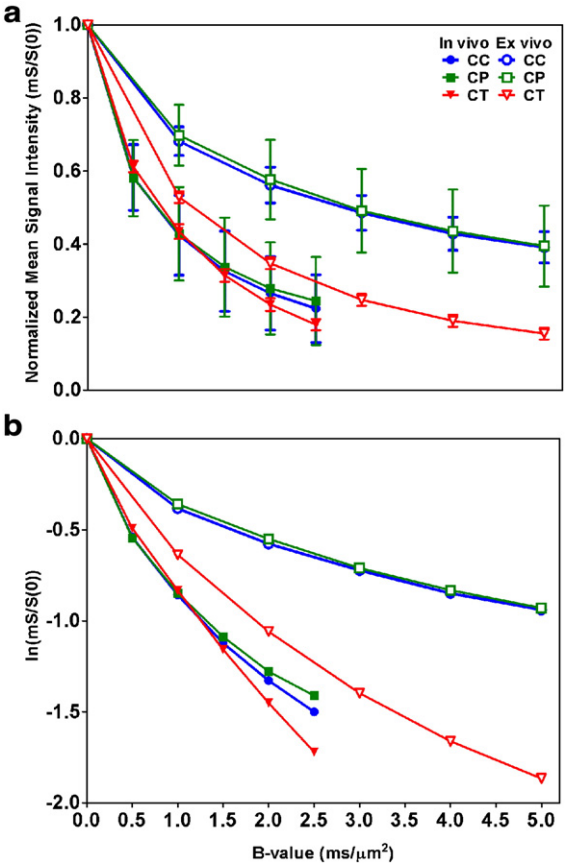

Fig. 4. Normalized (a) mean DW signal intensity (mS/S(0)) and (b) ln(mS/S(0)) vs. b-values in corpus callosum (CC), cerebral peduncle (CP) and cerebral cortex (CT). DW signals were measured from slice I of the in vivo and formalin-fixed ex vivo rat brains shown in Figs. 1 and 2. The signal intensity is the average DW signal in all 30 directions. Error bar represents the standard deviation in 30 directions.

formalin-fixed condition (Fig. 2f). Interestingly, the FA_K maps were found to closely resemble the FA maps under both conditions.

To illustrate the kurtosis contrast behavior, the normalized mean signal intensity vs. b-value is plotted in Fig. 4 for three representative ROIs in slice I of the in vivo and ex vivo rat brains shown in Figs. 1 and 2. Note that the mean signal intensity was obtained by averaging the DW signals in 30 directions. The error bar shows the standard deviation (SD) of these DW signals. The decay of the mean DW signals in WM for CC and CP in vivo was clearly non-monoexponential as a result of the water diffusion restriction caused by axonal membranes and myelin sheath (Assaf and Cohen, 2000; Beaulieu, 2002). Such decay behavior gave rise to directional kurtosis $K_{//}$ and $K\perp$ of 0.61 and 1.64, and 0.62 and 1.75, respectively, for CC and CP in this animal. On the other hand, $K_{//}$ and $K\perp$ in GM for CT were estimated to be 0.71 and 0.83 respectively. This $K\perp$ reduction in CT likely resulted from the less overall diffusion restriction in all directions given the relatively isotropic cell body structure of neurons being more densely packed in GM. In addition, the SDs of DW signals of in vivo CC and CP were much higher than those of CT for all b-values due to anisotropic diffusion and restriction, producing high FA values of 0.61 and 0.64, and high FA_K values of 0.45 and 0.48, respectively, in CC and CP. In contrast, FA and FA_K of CT were estimated as 0.17 and 0.12, respectively.

ROI quantifications of various brain tissues in vivo and ex vivo

Fig. 5 shows the typical ROI selection of various brain tissues for the quantitative DKI and DTI analysis. The ROIs selected for CC, EC, CP, AC, CT, HP and CPu typically contained 20±3, 53±8, 23±5, 6±2, 680±106, 300±46 and 740±77 reconstructed image voxels, respectively. Note that the ROI for each tissue was typically covered in one to three coronal slices. Fig. 6 shows the DTI and DKI estimates for these neural tissues as measured from all in vivo and ex vivo brains studied. Numerical values and their differences between in vivo and ex vivo experiments are tabulated

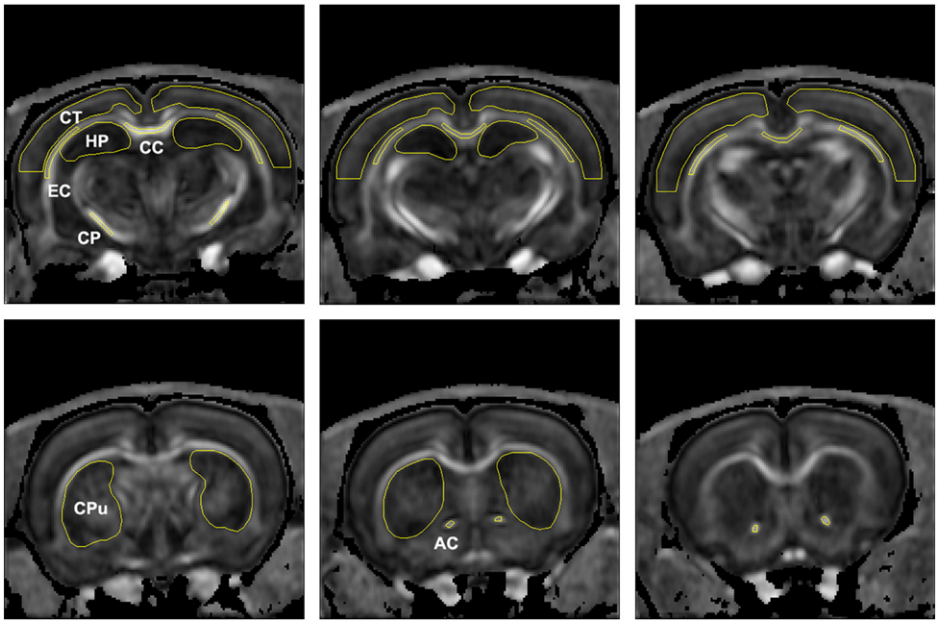

Fig. 5. Illustration of the typical ROI definitions used to quantify the DTI and DKI parameters. Four WM ROIs are corpus callosum (CC), external capsule (EC), cerebral peduncle (CP) and anterior commissure (AC). Three GM ROIs are cerebral cortex (CT), hippocampus (HP) and cauduate putamen (CPu).

in Table 1. Note that positive values were found for all mean and directional kurtoses, meaning that the diffusion profiles in neural tissues were more sharply peaked than Gaussian distribution, thus indicating restricted, i.e., not free, diffusion environments under both in vivo and formalin fixed conditions. For DTI estimates, dramatic reductions in *MD*, $\lambda_{//}$ and $\lambda\perp$ were observed under formalin fixation for all GM and WM tissues with *FA* being largely preserved, consistent with the previous findings by others (Clark et al., 2002; Sun et al., 2005). For DKI estimates, kurtosis increase was observed for all WM and GM tissues under formalin fixation. $K\perp$ was seen generally higher than $K_{//}$ for each specific tissue, particularly in WM. CP showed the highest *MK* and $K\perp$. GM tissues exhibited relatively low kurtoses with $K_{//}$ and $K\perp$ being similar. However, these increases were seen much substantial in WM than in GM and more along the axial direction. Under in vivo condition, the highest $\lambda\perp$ and lowest $K\perp$ were found in HP. With formalin fixation, CT gave the highest $\lambda\perp$ and lowest $K\perp$. Under both conditions, the lowest $\lambda\perp$ and highest $K\perp$ were seen in CP. In addition, the trend of FA_K for different tissues in vivo and ex vivo was found to be similar to that of *FA* though it yielded a slightly narrower range.

DTI estimates vs. DKI estimates

Fig. 7 shows the scatter plots in diffusivity- and kurtosis-space for various tissues among the individual in vivo and ex vivo brains studied. Different neural tissues occupy different locations with certain extents of overlap. Under both conditions, GM tissues can be separated from WM tissues in both diffusivity and kurtosis spaces. In particular, $K\perp$ shows the best differentiating capability among all directional diffusivities and kurtoses, underscoring the usefulness of directional kurtosis analysis. To illustrate the tissue representation in

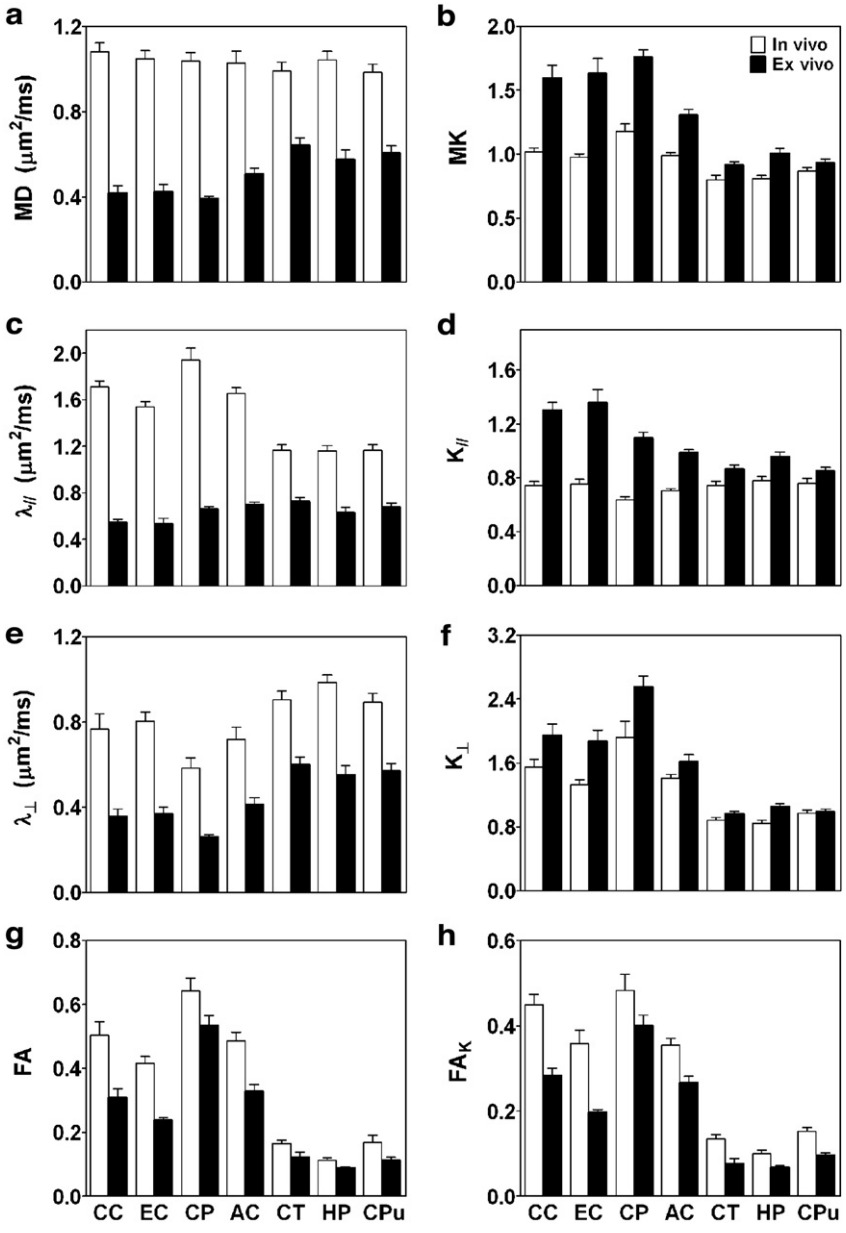

Fig. 6. DTI and DKI estimates measured for various neural tissues from in vivo adult rat brains ($N=7$) and formalin-fixed ex vivo adult rat brain samples ($N=5$).

Table 1
MD, $\lambda_{//}$, $\lambda_{\perp}$, *FA*, *MK*, $K_{//}$, $K_{\perp}$ and FA_K estimates (mean±standard deviation) of different anatomical structures

		MD	$\lambda_{//}$	$\lambda_{\perp}$	*FA*	*MK*	$K_{//}$	$K_{\perp}$	FA_K
		Mean±SD	Mean±SD	Mean±SD	Mean±SD	Mean±SD	Mean±SD	Mean±SD	Mean±SD
CC	In vivo	1.08±0.04	1.71±0.05	0.77±0.07	0.50±0.04	1.02±0.03	0.74±0.03	1.55±0.10	0.45±0.03
	Ex vivo	0.42±0.03	0.54±0.03	0.35±0.04	0.31±0.03	1.60±0.10	1.30±0.06	1.94±0.15	0.28±0.02
	% Difference	61.37**	68.21**	53.76**	38.71**	−56.54**	−75.97**	−25.68**	36.87**
EC	In vivo	1.05±0.04	1.54±0.05	0.80±0.04	0.42±0.02	0.97±0.03	0.75±0.04	1.33±0.07	0.36±0.03
	Ex vivo	0.42±0.03	0.53±0.04	0.37±0.03	0.24±0.01	1.63±0.12	1.36±0.10	1.87±0.14	0.20±0.01
	% Difference	59.49**	65.23**	54.00**	42.87**	−67.44**	−80.44**	−41.24**	44.95**
CP	In vivo	1.04±0.04	1.94±0.11	0.58±0.05	0.64±0.04	1.18±0.06	0.63±0.03	1.92±0.21	0.48±0.04
	Ex vivo	0.39±0.01	0.66±0.02	0.26±0.01	0.53±0.03	1.76±0.06	1.09±0.04	2.56±0.13	0.40±0.02
	% Difference	62.12**	66.06**	55.57**	16.80**	−49.40**	−72.38**	−33.27**	17.01**
AC	In vivo	1.03±0.05	1.65±0.05	0.72±0.06	0.49±0.03	0.99±0.02	0.70±0.02	1.41±0.05	0.35±0.02
	Ex vivo	0.51±0.03	0.7±0.02	0.41±0.03	0.33±0.02	1.31±0.05	0.99±0.02	1.62±0.09	0.27±0.02
	% Difference	50.70**	57.80**	42.52**	32.66**	−32.09**	−40.83**	−14.71**	24.84**
CT	In vivo	0.99±0.04	1.16±0.05	0.90±0.04	0.16±0.01	0.80±0.04	0.74±0.03	0.89±0.04	0.13±0.01
	Ex vivo	0.64±0.03	0.73±0.03	0.60±0.03	0.12±0.02	0.91±0.03	0.86±0.03	0.97±0.03	0.08±0.01
	% Difference	35.23**	37.66**	33.67**	25.76**	−14.34**	−16.37**	−9.11*	42.78**
HP	In vivo	1.04±0.04	1.16±0.05	0.98±0.04	0.11±0.01	0.81±0.03	0.78±0.03	0.85±0.03	0.10±0.01
	Ex vivo	0.58±0.05	0.63±0.05	0.55±0.04	0.09±0.00	1.01±0.04	0.95±0.04	1.05±0.04	0.07±0.00
	% Difference	44.71**	45.96**	43.97**	20.95**	−24.91**	−22.72**	−23.87**	31.67**
CPu	In vivo	0.98±0.04	1.16±0.05	0.89±0.04	0.17±0.02	0.87±0.03	0.76±0.03	0.97±0.04	0.15±0.01
	Ex vivo	0.60±0.04	0.68±0.04	0.57±0.04	0.11±0.01	0.93±0.03	0.85±0.03	0.99±0.03	0.10±0.01
	% Difference	38.48**	41.92**	36.24**	32.74**	−7.54*	−11.93**	−2.11	37.19**

Percentage difference of all estimates from in vivo to ex vivo was also shown.
* $p<0.05$.
** $p<0.01$.

both diffusivity and kurtosis spaces, Fig. 8 gives the scatter plots for all neural tissue pixels within the single in vivo and ex vivo brains shown in Fig. 1 and Fig. 2, respectively. The overall trends are similar to those in Fig. 7. Note that such pixel-based plotting circumvents the issue of inter-sample variation in ROI delineations.

Fig. 9 shows the correlation scatter plots between various DKI and DTI estimates measured for the WM and GM tissues, namely, *MK* vs. *MD*, $K_{//}$ vs. $\lambda_{//}$, $K_{\perp}$ vs. $\lambda_{\perp}$, and FA_K vs. *FA*. Note that the correlation coefficients were calculated using Spearman-rho analysis, i.e., without any assumption about the distribution of the measurements. Between *MK* and *MD*, no significant correlation ($r=0.44$) was observed in vivo while a strong correlation ($r=-0.98$, $p<0.0001$) existed ex vivo. Negative correlations were observed between directional kurtosis and diffusivity, particularly

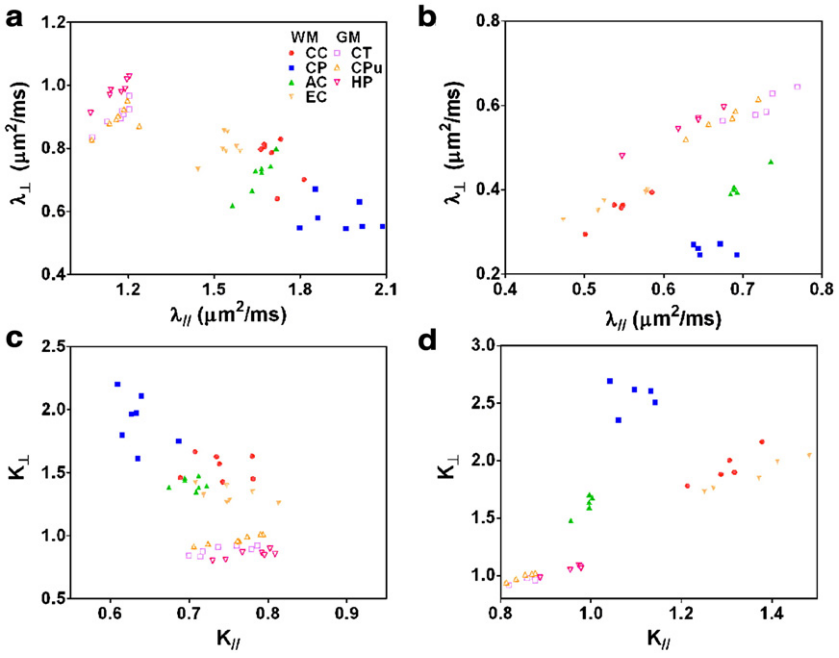

Fig. 7. Scatter plots of the directional diffusivities ($\lambda_{\perp}$ vs. $\lambda_{//}$) and directional kurtoses ($K_{\perp}$ vs. $K_{//}$) measured for various neural tissues from 7 in vivo brains (left column) and 5 ex vivo brains (right column).

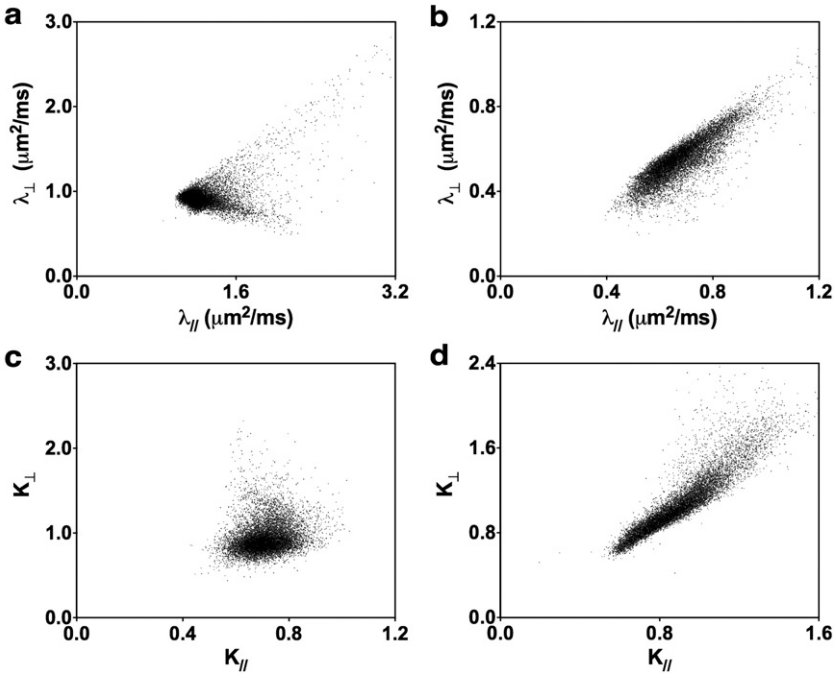

Fig. 8. Scatter plots of the directional diffusivity and kurtosis estimates for all neural tissue pixels within the single in vivo (left column) and ex vivo (right column) brains shown in Figs. 1 and 2, respectively.

between $K\perp$ and $\lambda\perp$. They were found stronger ex vivo, and were even stronger if only WM tissues were considered. As for FA_K vs. FA, strong correlations were found for all tissues under in vivo ($r=0.92$, $p<0.0001$) and ex vivo ($r=0.95$, $p<0.0001$) conditions, leading to marked similarity in contrast between FA and FA_K maps as seen in Figs. 1 and 2. Fig. 10 shows the corresponding scatter plots for all neural tissue pixels within the single in vivo and ex vivo brains in Figs. 1 and 2. They exhibit trends similar to those in Fig. 9, again indicating that DKI and DTI estimates were correlated but also different particularly under in vivo condition.

Discussions

Numerous DTI studies have been performed successfully by utilizing the directional diffusion analysis to detect and monitor various pathophysiological changes in neural tissues, including brain and spinal cord (Basser and Pierpaoli, 1996; Kim et al., 2007; Song et al., 2003; Sun et al., 2006). Water molecule diffusion in vivo is a complex process with restriction incurred by numerous determinants such as intra-/extracellular compartments, permeability or water exchange, and potentially other biophysical properties associated with different water populations. Such biophysical complexity underscores the importance of investigating the restrictive diffusion environments in order to provide a more sensitive and specific MR characterization of neural tissues, including both WM and GM tissues. With DKI, information regarding the extent of water diffusion restriction can be obtained. In spite of the absence of any directional analysis, recent DKI studies have demonstrated that mean kurtosis yields useful diffusion information, offering sensitivity superior to that of the conventional DTI in detecting certain neural pathologies (Falangola et al., 2007a,b; Helpern et al., 2007; Ramani et al., 2007). Given these developments, the need emerges for directional analysis of diffusion kurtosis. The orthogonal transformation of the 4th order diffusion kurtosis tensor was formulated in the current study to compute the directional kurtoses so as to probe the deviation of water diffusion from Gaussian distribution in the local coordinates inherent to the 2nd order diffusion eigenvectors. Directional kurtosis analysis was shown to give different and complimentary measurements, indicating that such analysis can enhance MR diffusion characterization of various neural tissues and detection of their pathophysiological changes.

Diffusion kurtosis analysis of WM and GM tissues in vivo

In the current study, negative correlations were generally observed between directional kurtosis and diffusivity. This is largely expected given that the high kurtosis or restricted diffusion is often associated with or leads to a low diffusion rate. However, such correlation cannot rule out the unique and supplementary information provided by DKI because DKI and DTI estimates were derived together using Eq. (1) as two separate estimates from the DW signal decays as a function of multiple b-values and diffusion directions. This could be observed in our experimental DKI and DTI results. For example, $\lambda_{//}$ was not found to follow the same trend as that of $K_{//}$ in vivo as shown in Figs. 6c and d. In vivo $K_{//}$ was largely the same for all tissues while $\lambda_{//}$ differed between GM and WM. In addition, the extent of correlations between DKI and DTI estimates was substantially less in vivo as seen in Figs. 9 and 10, underscoring the in vivo biophysical complexity of water diffusion restriction and the need to probe it.

In vivo WM microstructure is often simplified as the ordered axons that contain neurofibrils such as microtubules and neurofilaments, which are wrapped by myelin (Beaulieu, 2002). As a result, one would expect the in vivo diffusion environment along the axonal direction could be rather homogeneous, thus leading to less diffusion restriction and lower $K_{//}$ than in GM. However, this is not the case. As shown in Fig. 6(d), WM and GM exhibited similar $K_{//}$ values in vivo. Such diffusion restriction in WM along the axonal or axial

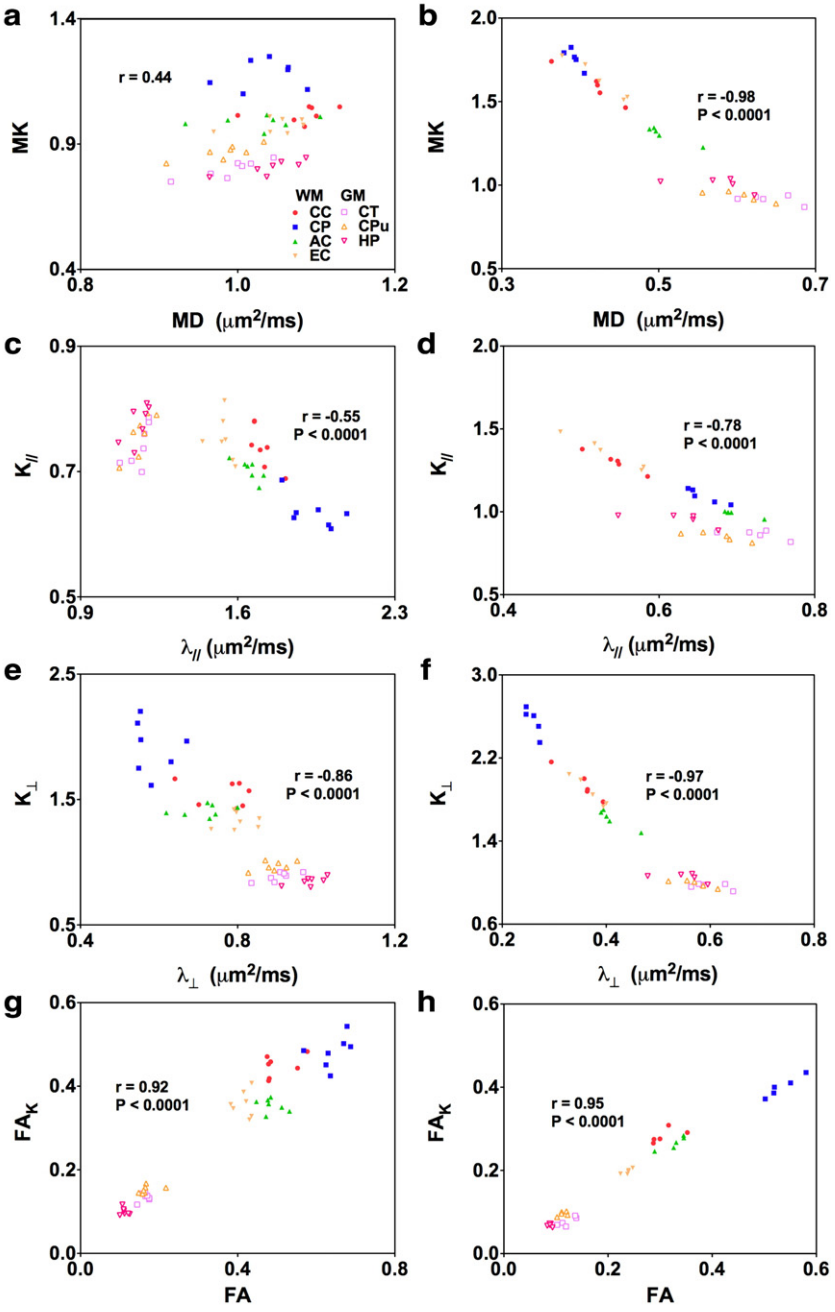

Fig. 9. Spearman-rho correlations between various DKI and DTI estimates measured for various neural tissues from 7 in vivo brains (left column) and 5 ex vivo brains (right column). The correlations were (a) and (b) *MK* vs. *MD*, (c) and (d) $K_{//}$ vs. $\lambda_{//}$, (e) and (f) $K\perp$ vs. $\lambda\perp$, and (g) and (f) FA_K vs. *FA*. Note that symbols with the same color were the estimate from different animals.

direction may be ascribed to the presence of membranes of the glial cells, astrocytes and oligodendrocytes (Waxman et al., 1995).

Diffusion kurtosis changes associated with formalin fixation

Our results indicated that water diffusion is more restricted under the formalin-fixed condition, as revealed by the general increase in *MK*, $K_{//}$ and $K\perp$. Fixatives are known to cause the breakdown of neurofilaments and microtubules (Does et al., 2003; Schwartz et al., 2005; Takahashi et al., 2002; Thelwall et al., 2006; Yong-Hing et al., 2005), possibly producing more diffusion barriers. Such microstructural changes may lead to the $\lambda_{//}$ decrease and $K_{//}$ increase. They may also partly account for the dramatic difference between the in vivo and ex vivo $K_{//}$ vs. $\lambda_{//}$ scatter plots (Figs. 9c and d). Moreover, fixation causes tissue shrinkage (Yong-Hing et al., 2005), significant decrease in membrane permeability (Thelwall et al., 2006), increase in axonal packing density (Takahashi et al., 2002) and reduction of extracellular space in parenchyma (Go, 1997). These changes likely play a role in the significant $\lambda\perp$ decreases and $K\perp$ increases observed in the current study. One noteworthy observation was the substantial $K_{//}$ increase (up to 80%) and yet only moderate $K\perp$ increase (up to 41%) in WM (Figs. 6d and f). Meanwhile, the percentages of $\lambda_{//}$ and $\lambda\perp$ decreases were seen to be similar (Figs. 6c and e). This finding

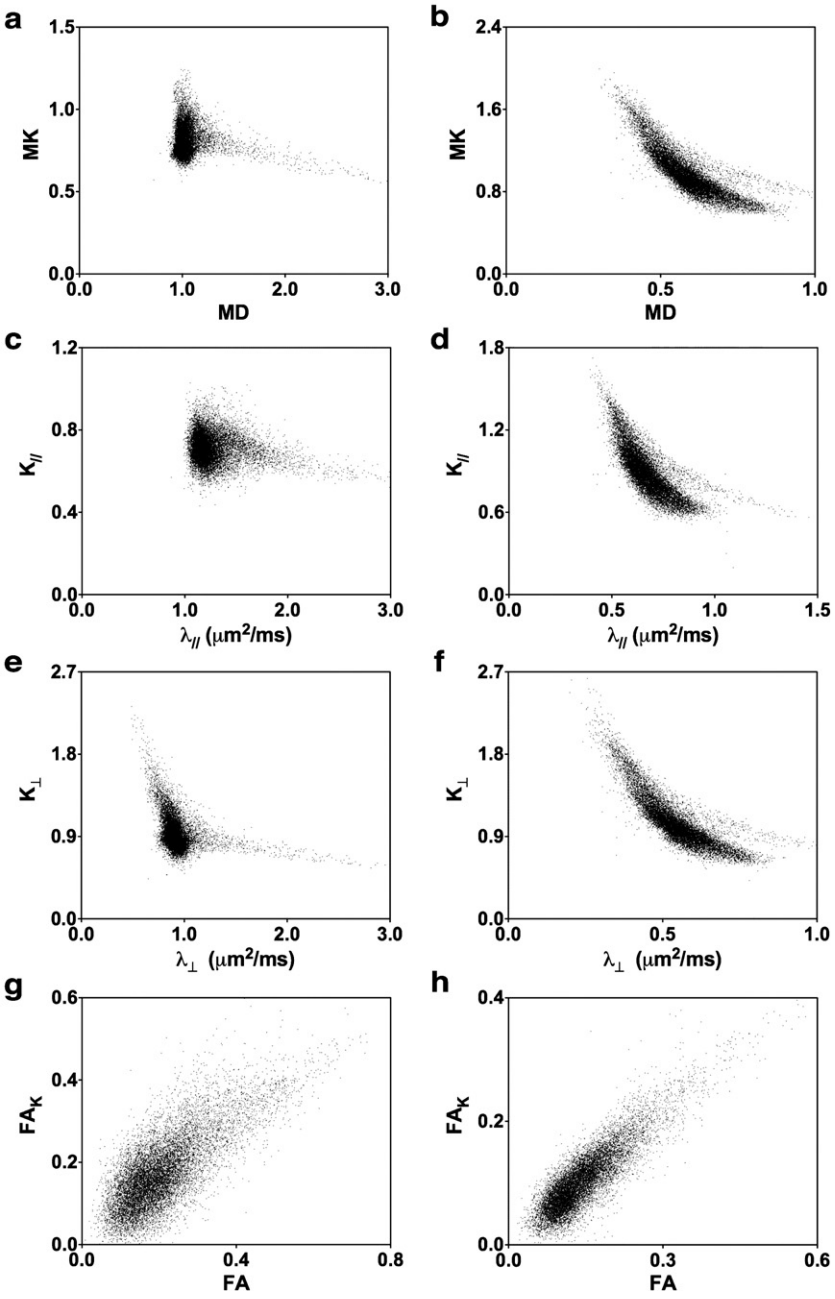

Fig. 10. Scatter plots of various DKI and DTI estimates for all neural tissue pixels within the single in vivo (left column) and ex vivo (right column) brains shown in Figs. 1 and 2.

indicates that fixation may produce more restrictive diffusion environment along the axonal direction. It is noteworthy that the diffusivity and kurtosis differences observed between in vivo to formalin-fixed conditions as seen in Figs. 6a, c and e may arise from the low temperature at which the brain samples were studied (20 °C ex vivo as compared to 37 °C in vivo). Diffusion is known to increase with temperature in an exponential manner (Quesson et al., 2000). A recent study has shown that *MD* in formalin-fixed primate brains increased by 60% and 95% in GM and WM, respectively, when temperature was raised from 24 °C to 44 °C (D'Arceuil et al., 2007). In fact, a simple DKI experiment was conducted in our lab in a formalin-fixed rat brain with temperature rising from 20 °C and 35 °C. *MD* increases of ~51% and ~68% were observed in GM and WM, respectively. Meanwhile, *MK* was observed to decrease by ~12% and ~15%, respectively, indicating a less restrictive diffusion environment at high temperature in fixated neural tissues.

Combined diffusion and kurtosis analysis

In the current study, DTI and DKI estimate were documented for various WM and GM tissues in adult rat brains in vivo and ex vivo. The diffusivity values shown in Table 1 are generally higher than those previously reported using single *b*-value measurement (Harsan et al., 2006), particularly for WM $\lambda\perp$. This discrepancy resulted from the fact that the apparent diffusion and kurtosis were derived together by fitting the multiple *b*-value DW signal decays to Eq. (1). The early

DW signal decays in Fig. 4 were dominated by the first term ($-bD_{app}$) in Eq. (1), which contributed most to the D_{app} estimation. These early decay points were acquired with *b*-values (500 s/mm^2 and 1000 s/mm^2 for in vivo and ex vivo DKI, respectively) that were smaller than those single *b*-values typically used in the conventional DTI. As seen in Fig. 4, DW signals exhibited stronger decays at small *b*-values, thus leading to larger diffusivity estimations. Note that the *FA* values were also slightly lower. Such *b*-value dependency of the conventional DTI estimates again underscores their methodological limitation in quantitative tissue characterization.

On the other hand, DKI approach also has its own potential limitations. Unlike in q-space imaging where diffusion profile is fully measured, DKI only measures the 4th central moment of the diffusion profile, i.e., diffusion kurtosis. It utilizes the well-known non-monoexponential *b*-value dependency of DW signals in neural tissues, serving as the 1st order assessment of the deviation from the free or Gaussian diffusion behavior. In addition, Eq. (1) consists of only two terms to relate DW signal decay to *b*-value, namely diffusivity and kurtosis in contrast to the expansion series in the framework of generalized diffusion tensor (Liu et al., 2004; Ozarslan and Mareci, 2003). Thus the quantitative accuracy of estimating the apparent diffusion coefficient and diffusion kurtosis from the two truncated terms in Eq. (1) remains to be validated. Nevertheless, the current study demonstrated that DKI analysis revealed information that was independently estimated and different from the conventional diffusivity estimates. Therefore, the combined and multi-parametric analysis of various directional diffusivities and kurtoses will improve the tissue characterization over the diffusivity analysis alone though the optimal analysis strategy and validations remain to be investigated.

Conclusions

Directional diffusion kurtosis analysis was presented to study the non-Gaussian diffusion behavior along the three eigenvectors of the conventional diffusion tensor. Radial and axial kurtoses were derived for the first time and applied to DKI study of rodent brains under in vivo and formalin-fixed conditions. Various kurtosis estimates were documented for WM and GM tissues, and compared to the diffusion tensor estimates. The results demonstrated that kurtosis estimates can reveal different information from the conventional diffusivity estimates, thus could be valuable in characterizing neural tissues and detecting their microstructural alterations.

Acknowledgments

The authors would like to thank Drs. Jens H. Jensen and Joseph A. Helpern at New York University School of Medicine in New York, and Dr. Hanzhang Lu at UT Southwestern Medical Center in Dallas for providing assistance with data processing procedures. This work was supported in part by the University of Hong Kong Committee on Research and Conference Grants and Hong Kong Research Grant Council.

References

Assaf, Y., Cohen, Y., 2000. Assignment of the water slow-diffusing component in the central nervous system using q-space diffusion MRS: implications for fiber tract imaging. Magn. Reson. Med. 43, 191–199.

Assaf, Y., Mayk, A., Eliash, S., Speiser, Z., Cohen, Y., 2003. Hypertension and neuronal degeneration in excised rat spinal cord studied by high-b value q-space diffusion magnetic resonance imaging. Exp. Neurol. 184, 726–736.

Assaf, Y., Chapman, J., Ben-Bashat, D., Hendler, T., Segev, Y., Korczyn, A.D., Graif, M., Cohen, Y., 2005. White matter changes in multiple sclerosis: correlation of q-space diffusion MRI and 1H MRS. Magn. Reson. Imaging 23, 703–710.

Balanda, K.P., Macgillivray, H.L., 1988. Kurtosis — a critical review. American Statistician 42, 111–119.

Basser, P.J., Jones, D.K., 2002. Diffusion-tensor MRI: theory, experimental design and data analysis — a technical review. NMR Biomed. 15, 456–467.

Basser, P.J., Pierpaoli, C., 1996. Microstructural and physiological features of tissues elucidated by quantitative-diffusion-tensor MRI. J. Magn. Reson. B 111, 209–219.

Basser, P.J., Mattiello, J., LeBihan, D., 1994. MR diffusion tensor spectroscopy and imaging. Biophys. J. 66, 259–267.

Beaulieu, C., 2002. The basis of anisotropic water diffusion in the nervous system — a technical review. NMR Biomed. 15, 435–455.

Biton, I.E., Duncan, I.D., Cohen, Y., 2006. High b-value q-space diffusion MRI in myelin-deficient rat spinal cords. Magn. Reson. Imaging 24, 161–166.

Callaghan, P.T., 1991. Principles of nuclear magnetic resonance microscopy. Oxford University Press, Oxford England.

Clark, C.A., Hedehus, M., Moseley, M.E., 2002. In vivo mapping of the fast and slow diffusion tensors in human brain. Magn. Reson. Med. 47, 623–628.

D'Arceuil, H.E., Westmoreland, S., de Crespigny, A.J., 2007. An approach to high resolution diffusion tensor imaging in fixed primate brain. Neuroimage 35, 553–565.

Does, M.D., Parsons, E.C., Gore, J.C., 2003. Oscillating gradient measurements of water diffusion in normal and globally ischemic rat brain. Magn. Reson. Med. 49, 206–215.

Falangola, M.F., Branch, C., Jensen, J.H., Hu, C., Xuan, L., Duff, K., Nixon, R., Helpern, J.A., 2007a. Assessment of brain microstructure in a transgenic mouse model of β-amyloid deposition. Proceedings of the 15th Annual Meeting of ISMRM, Berlin, Germany, p. 310.

Falangola, M.F., Ramani, A., Dl Martino, A., Jensen, J.H., Babb, J.S., Hu, C., Szulc, K.U., Castellanos, F.X., Helpern, J.A., 2007b. Age-related patterns of change in brain microstructure by diffusional kurtosis imaging. Proceedings of the 15th Annual Meeting of ISMRM, Berlin, Germany, p. 667.

Fieremans, E., De Deene, Y., Delputte, S., Ozdemir, M.S., D'Asseler, Y., Vlassenbroeck, J., Deblaere, K., Achten, E., Lemahieu, I., 2008. Simulation and experimental verification of the diffusion in an anisotropic fiber phantom. J. Magn. Reson. 190, 189–199.

Go, K.G., 1997. The normal and pathological physiology of brain water. Adv. Tech. Stand. Neurosurg. 23, 47–142.

Harsan, L.A., Poulet, P., Guignard, B., Steibel, J., Parizel, N., de Sousa, P.L., Boehm, N., Grucker, D., Ghandour, M.S., 2006. Brain dysmyelination and recovery assessment by noninvasive in vivo diffusion tensor magnetic resonance imaging. J. Neurosci. Res. 83, 392–402.

Helpern, J.A., Falangola, M.F., Dl Martino, A., Ramani, A., Babb, J.S., Hu, C., Jensen, J.H., Castellanos, F.X., 2007. Alterations in brain microstructure in ADHD by diffusional kurtosis imaging. Proceedings of the 15th Annual Meeting of ISMRM, Berlin, Germany, p. 1580.

Jensen, J.H., Helpern, J.A., Ramani, A., Lu, H., Kaczynski, K., 2005. Diffusional kurtosis imaging: the quantification of non-gaussian water diffusion by means of magnetic resonance imaging. Magn. Reson. Med. 53, 1432–1440.

Jones, D.K., Horsfield, M.A., Simmons, A., 1999. Optimal strategies for measuring diffusion in anisotropic systems by magnetic resonance imaging. Magn. Reson. Med. 42, 515–525.

Karger, J., 1985. NMR self-diffusion studies in heterogeneous systems. Adv. Colloid Interface Sci. 23, 129–148.

Kim, J.H., Loy, D.N., Liang, H.F., Trinkaus, K., Schmidt, R.E., Song, S.K., 2007. Noninvasive diffusion tensor imaging of evolving white matter pathology in a mouse model of acute spinal cord injury. Magn. Reson. Med. 58, 253–260.

Le Bihan, D., 1991. Molecular diffusion nuclear magnetic resonance imaging. Magn. Reson. Q. 7, 1–30.

Liu, C., Bammer, R., Acar, B., Moseley, M.E., 2004. Characterizing non-Gaussian diffusion by using generalized diffusion tensors. Magn. Reson. Med. 51, 924–937.

Lu, H., Jensen, J.H., Ramani, A., Helpern, J.A., 2006. Three-dimensional characterization of non-gaussian water diffusion in humans using diffusion kurtosis imaging. NMR Biomed. 19, 236–247.

Mulkern, R.V., Gudbjartsson, H., Westin, C.F., Zengingonul, H.P., Gartner, W., Guttmann, C.R., Robertson, R.L., Kyriakos, W., Schwartz, R., Holtzman, D., Jolesz, F.A., Maier, S.E., 1999. Multi-component apparent diffusion coefficients in human brain. NMR Biomed. 12, 51–62.

Niendorf, T., Dijkhuizen, R.M., Norris, D.G., van Lookeren Campagne, M., Nicolay, K., 1996. Biexponential diffusion attenuation in various states of brain tissue: implications for diffusion-weighted imaging. Magn. Reson. Med. 36, 847–857.

Nossin-Manor, R., Duvdevani, R., Cohen, Y., 2007. Spatial and temporal damage evolution after hemi-crush injury in rat spinal cord obtained by high b-value q-space diffusion magnetic resonance imaging. J. Neurotrauma 24, 481–491.

Ozarslan, E., Mareci, T.H., 2003. Generalized diffusion tensor imaging and analytical relationships between diffusion tensor imaging and high angular resolution diffusion imaging. Magn. Reson. Med. 50, 955–965.

Paxinos, G., Watson, C., 2005. The Rat Brain in Stereotaxic Coordinates — The New Coronal Set, 5th edition. Elsevier Academic Press, San Diego.

Qi, L.Q., 2005. Eigenvalues of a real supersymmetric tensor. J. Symb. Comput. 40, 1302–1324.

Qi, L., Wang, Y., Wu, E.X., in press. D-eigenvalues of diffusion kurtosis tensors. Journal of Computational and Applied Mathematics. doi:10.1016/j.cam.2007.10.012.

Quesson, B., de Zwart, J.A., Moonen, C.T., 2000. Magnetic resonance temperature imaging for guidance of thermotherapy. J. Magn. Reson. Imaging 12, 525–533.

Ramani, A., Jensen, J.H., Szulc, K.U., Ali, O., Hu, C., Lu, H., Brodle, J.D., Helpern, J.A., 2007. Assessment of abnormalities in the cerebral microstructure of schizophrenia patients: a diffusional kurtosis imaging study. Proceedings of the 15th Annual Meeting of ISMRM, Berlin, Germany, p. 648.

Schwartz, E.D., Cooper, E.T., Chin, C.L., Wehrli, S., Tessler, A., Hackney, D.B., 2005. Ex vivo evaluation of ADC values within spinal cord white matter tracts. AJNR Am. J. Neuroradiol. 26, 390–397.

Song, S.K., Sun, S.W., Ramsbottom, M.J., Chang, C., Russell, J., Cross, A.H., 2002. Dysmyelination revealed through MRI as increased radial (but unchanged axial) diffusion of water. Neuroimage 17, 1429–1436.

Song, S.K., Sun, S.W., Ju, W.K., Lin, S.J., Cross, A.H., Neufeld, A.H., 2003. Diffusion tensor imaging detects and differentiates axon and myelin degeneration in mouse optic nerve after retinal ischemia. Neuroimage 20, 1714–1722.

Sun, S.W., Neil, J.J., Song, S.K., 2003. Relative indices of water diffusion anisotropy are equivalent in live and formalin-fixed mouse brains. Magn. Reson. Med. 50, 743–748.

Sun, S.W., Neil, J.J., Liang, H.F., He, Y.Y., Schmidt, R.E., Hsu, C.Y., Song, S.K., 2005. Formalin fixation alters water diffusion coefficient magnitude but not anisotropy in infarcted brain. Magn. Reson. Med. 53, 1447–1451.

Sun, S.W., Liang, H.F., Trinkaus, K., Cross, A.H., Armstrong, R.C., Song, S.K., 2006. Noninvasive detection of cuprizone induced axonal damage and demyelination in the mouse corpus callosum. Magn. Reson. Med. 55, 302–308.

Takahashi, M., Hackney, D.B., Zhang, G., Wehrli, S.L., Wright, A.C., O'Brien, W.T., Uematsu, H., Wehrli, F.W., Selzer, M.E., 2002. Magnetic resonance microimaging of intraaxonal water diffusion in live excised lamprey spinal cord. Proc. Natl. Acad. Sci. U. S. A. 99, 16192–16196.

Thelwall, P.E., Shepherd, T.M., Stanisz, G.J., Blackband, S.J., 2006. Effects of temperature and aldehyde fixation on tissue water diffusion properties, studied in an erythrocyte ghost tissue model. Magn. Reson. Med. 56, 282–289.

Trip, S.A., Wheeler-Kingshott, C., Jones, S.J., Li, W.Y., Barker, G.J., Thompson, A.J., Plant, G.T., Miller, D.H., 2006. Optic nerve diffusion tensor imaging in optic neuritis. Neuroimage 30, 498–505.

Waxman, S.G., Kocsis, J.D., Stys, P.K., 1995. The Axon: structure, function, and pathophysiology. Oxford University Press, New York.

Woods, R.P., Grafton, S.T., Holmes, C.J., Cherry, S.R., Mazziotta, J.C., 1998. Automated image registration: I. General methods and intrasubject, intramodality validation. J. Comput. Assist. Tomogr. 22, 139–152.

Yablonskiy, D.A., Bretthorst, G.L., Ackerman, J.J., 2003. Statistical model for diffusion attenuated MR signal. Magn. Reson. Med. 50, 664–669.

Yong-Hing, C.J., Obenaus, A., Stryker, R., Tong, K., Sarty, G.E., 2005. Magnetic resonance imaging and mathematical modeling of progressive formalin fixation of the human brain. Magn. Reson. Med. 54, 324–332.